Advances in Geo-Energy Research

Vol. 8, No. 3, p. 146-158, 2023

Original article

Dynamic mechanisms of tight gas accumulation and numerical simulation methods: Narrowing the gap between theory and field application

Wen Zhao[1], Chengzao Jia[1,2]*, Yan Song[1,3]*, Xiangfang Li[3], Lianhua Hou[1], Lin Jiang[1]

[1]*Research Institute of Petroleum Exploration and Development, PetroChina, Beijing 100083, P. R. China*

[2]*PetroChina Company Ltd., Beijing 100011, P. R. China*

[3]*State Key Laboratory of Petroleum Resources and Prospecting, China University of Petroleum, Beijing 102249, P. R. China*

Keywords:
Tight gas reservoir
dynamic mechanisms
numerical simulation
upscaling

Cited as:
Zhao, W., Jia, C., Song, Y., Li, X., Hou, L., Jiang, L. Dynamic mechanisms of tight gas accumulation and numerical simulation methods: Narrowing the gap between theory and field application. Advances in Geo-Energy Research, 2023, 8(3): 146-158.
https://doi.org/10.46690/ager.2023.06.02

Abstract:
Despite the significant progress made in tight gas exploration and development in recent years, the understanding of the dynamic mechanisms of tight gas accumulation is still limited, and numerical simulation methods are lacking. In fact, the gap between theory and field application has become an obstacle to the development of tight gas exploration and development. This work sheds light on the dynamic mechanisms of hydrocarbon accumulation in tight formations from the aspect of capillary self-sealing theory by embedding calculation of pressure- and temperature-dependent capillary force in a pore network model. The microscale dynamic mechanisms are scaled up to the reservoir level by geological simulation, and the quantitative evaluation of reserves based on real geological sections is realized. From the results, several considerations are made to assist with resource assessment and sweet spot prediction. Firstly, the self-sealing effect of capillary in the micro-nano pore-throat system is at the core of tight sandstone gas accumulation theory; the hydrocarbon-generated expansion force is the driving force, and capillary force comprises the resistance. Furthermore, microscopic capillary force studies can be embedded into a pore network model and scaled up to a geological model using relative permeability curve and capillary force curve. Field application can be achieved by geological numerical simulations at the reservoir scale. Finally, high temperature and high pressure can reduce capillary pressure, which increases gas saturation and reserves.

1. Introduction

Tight sandstone gas plays a prominent role in unconventional resource exploration and development (Zhao et al., 2020; Pang et al., 2021). Recently, a massive increase in the production of tight gas around the world has been witnessed, such as in North America (Soleymanzadeh et al., 2021) and China (Jia et al., 2021). However, the research on hydrocarbon migration and accumulation dynamic mechanisms and multi-scale numerical simulation methods is still inadequate (Zhao et al., 2021), which poses an obstacle to the further exploration and development of tight gas.

The earliest report of tight sandstone gas can be traced to the North American Arapachian Basin. Emmons (1921a) noted that "many researchers at the Pennsylvania Geological Survey opposed the anticline theory, believing that much natural gas was in synclines." This indicates that these unconventional gas accumulations did not align with the anticlinal theory. However, no relevant geological theories have been developed to explain them, and these gas fields were not developed during that time (Emmons, 1921b; Wang et al., 2022). During the early stages of deep drilling in North America, such reservoirs were found in the Appalachia Basin (Sell et al., 2011), Anadarko Basin (Hentz, 1994), Fort Worth Basin (Thomas and Texas, 2002), and San Juan Basin (Fassett and Hinds,

Yandy Scientific Press

*Corresponding author.
E-mail address: zhaow22@petrochina.com.cn (W. Zhao); jiacz@petrochina.com.cn (C. Jia); sya@petrochina.com.cn (Y. Song); lixf2013@vip.163.com (X. Li); houlh@petrochina.com.cn (L. Hou); jianglin01@petrochina.com.cn (L. Jiang).

Received April 26, 2023; revised May 14, 2023; accepted May 27, 2023; available online May 31, 2023.

1971). These gas accumulations were firstly interpreted as conventional stratigraphic or structural traps (Hills, 1968). However, as exploration and development progressed, the size of these early discovered gas fields became increasingly larger, as confirmed by new drilling operations (Fassett, 1991). It gradually became clear that the earlier anticlinal accumulation theory might no longer be applicable to such gas fields (Blanchard et al., 1968; Hu et al., 2022a). Some petroleum geologists have discussed the peculiarities of this gas reservoir type. In the Blanco gas field in the San Juan Basin, Budd (1959) noted that there was no clear dividing line between producing and nonproducing wells. It appeared that the porosity and permeability of the reservoir corresponding to each well controlled the production. During the development of Booneville gas field in the Fort Worth Basin, Blanchard et al. (1968) noted that structure had little impact on gas accumulation, and gas could still be produced in a single lens at low-structure sites. However, no new accumulation models were proposed at the time, and geologists only stated that "further understanding of the geological context of these gas accumulation types is needed" (Tissot and Welte, 1984).

In 1976, Canadian oil company discovered the Elmworth gas field in the deep and low depressions of the western Alberta Basin. In the same year, Masters (1979) proposed the concepts of deep basin gas traps and deep basin gas accumulation for tight sandstone gas reservoir (Zhang et al., 2022). Masters presented accumulation model at the AAPG annual meeting in 1984, and called on petroleum geologists to conduct further studies on the development of such reservoirs. These included studies on geochemistry (Sneider et al., 1978), logging lithology calibration (Davis, 1984), pressure (Jackson, 1984), regional sedimentary facies (Rahmani, 1984), production characteristics, and well drilling and completion (Smith, 1984). The tight sandstone gas reservoir was found to have two remarkable characteristics: (1) It is distributed in the low concave part of the center and edge of a basin or depression; (2) the reservoir is often a tight sand layer. Based on geologists' observation of the inversion of gas and water, this kind of gas reservoir is also called "tight sandstone gas accumulation" (Myers, 1984) or "water sealed sandstone gas accumulation" (Stayura, 1984). The distribution range of tight sand gas reservoir can extend from the deepest depression of the basin to the edge of the basin and contain large reserves, thereby some scholars call them "continuous gas accumulation". To sum up, under Master's leadership, petroleum geologists established a new accumulation model for the Alberta Basin (Law, 2002).

Recently, several advances have been made in this field, from the development of the "tank sealing theory" to the further study of capillary sealing (Rutter et al., 2022). Thus, petroleum geologists have developed a more profound understanding of tight sandstone gas reservoirs and established increasingly sophisticated models (Wang et al., 2020). With the development of the petroleum industry, the limits of the physical properties of reservoirs that can be exploited have become lower, and reservoir water saturation limits have increased (Burrows et al., 2020). Due to the complicated distribution relationship between gas and water in tight sandstone gas reservoirs, scientists need to focus on the micro-scale accumulation mechanism of tight gas (Khalifah et al., 2020). With the discovery of the Elmworth gas field in the Alberta Basin, in the 1970s, researchers began to discuss the accumulation conditions and sealing mechanism of tight sandstone gas reservoirs (Khatibi et al., 2019). Berry (1959) believed that the downward flow trend of formation water blocks the upward migration of natural gas under the action of buoyancy, preserving the gas reservoir (Li et al., 2021). However, Masters (1979) discounted the downward flow theory, suggesting that high water saturation in the formation creates a permeability barrier between the water and the gas phase. Shanley et al. (2004) studied the tight sandstone gas reservoirs that had been discovered by then. He believed that when the water saturation in the reservoir reaches 50% to 95%, the fluid in the reservoir has little relative permeability, irrespective of the water phase or the gas phase (Lin et al., 2017). Cluff and Byrnes (2010) recognized Byrnes' permeability dead zone and proposed the concept of "jail", that is, the relative permeability of natural gas in a reservoir with high water saturation is reduced to zero.

Despite the above research developments, many obstacles still limit the effective exploration and development of tight oil/gas, such as the poor understanding of accumulation mechanisms (Abukova et al., 2019; Hu et al., 2022b), the lack of quantitative simulation methods for hydrocarbon migration and accumulation processes (Blunt, 2017; Zhao et al., 2020), and difficulties associated with sweet spot prediction (Algarhy and Ibrahim, 2022; Gholami et al., 2022). In summary, the self-sealing effect of capillary pressure in a micro-nano pore throat system is at the core of tight sandstone gas accumulation theory (Jia et al. 2023), which prompts petroleum geologists to study capillary forces at a smaller scale and to use more advanced techniques and methods to simulate tight sandstone gas migration and accumulation process. To this end, this work reveals the dynamic mechanism of tight gas accumulation and provides a multiscale numerical simulation method to achieve the aforementioned simulation goal.

2. Geological setting

In this work, the Sulige tight gas field is taken as a typical tight sandstone gas reservoir (Fig. 1). According to the properties of the basement, geological evolution history and structural characteristics of the Ordos Basin, it can be divided into six structural units, namely, Yimeng Uplift, Yishan Slope, Tianhuan prospecting Depression, Jinxi Belt, western margin fold belt and Weibei Uplift. The Yishan Slope was formed at the end of the Early Bailian Period and is the largest first-order tectonic unit in the basin, with a width of 250 km from east to west and a length of 400 km from north to south. The present tectonic feature is a large gentle monocline with a westward dip, the average dip is about approximately 1°, and the dip angle is less than 1°.

The upper Paleozoic strata can be divided into Carboniferous Benxi (C_2b), Permian Taiyuan (P_1t), Shanxi (P_1s), lower Shihezi (P_2h), upper Shihezi (P_2h), and Shiqianfeng Formations (P_3q) (from bottom to top). The upper and lower Shihezi can be divided into eight gas-bearing strata (P_2h_1-

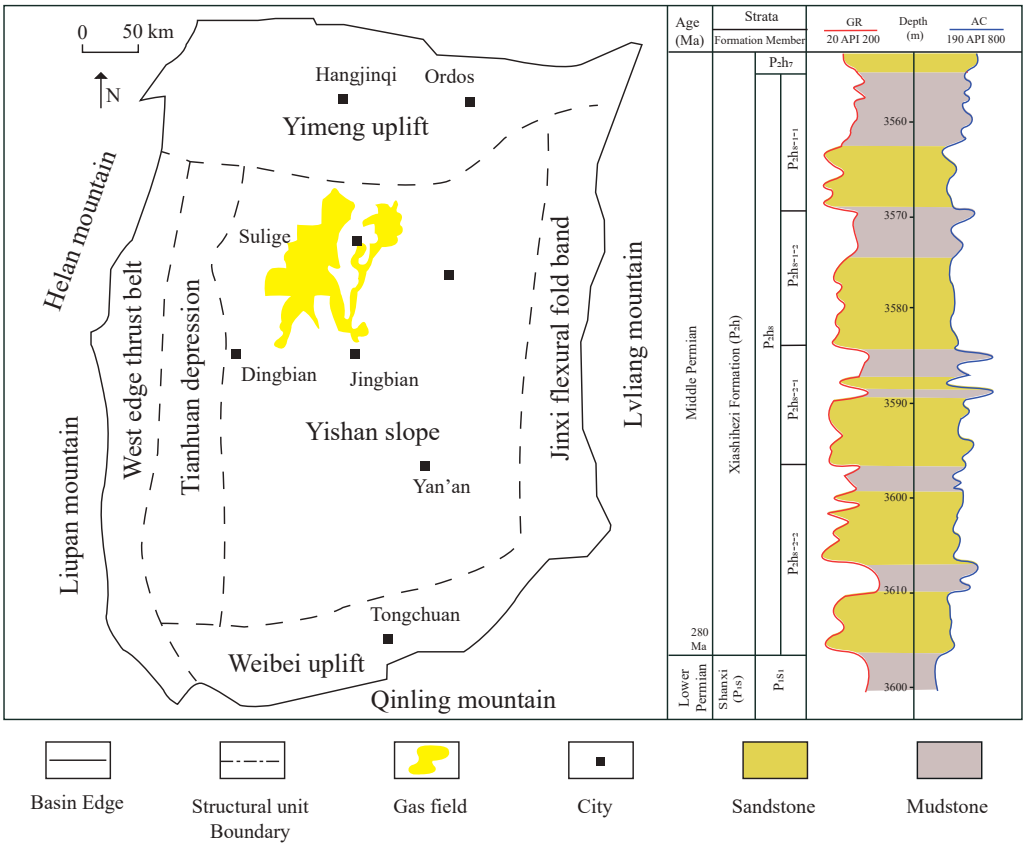

Fig. 1. Map of Sulige gas field in the Ordos Basin and sedimentary strata in the Shihezi Formation (Wu et al., 2021; Zhao et al., 2021).

P_2h_8, from top to bottom). The main reservoir stratum in the Sulige gas field is the P_2h_8 section in the lower Shihezi Formation, which can be further divided into four segments from top to bottom: P_2h_{8-1-1}, P_2h_{8-1-2}, P_2h_{8-2-1}, and P_2h_{8-2-2}, which are characterized by extensive distribution and strong heterogeneity. The coal source beds in the Sulige area are mainly developed in the Shan-2 Member Taiyuan Formation. The reservoirs mainly consist of the He-8 Member and Shan-1 Member. From the perspective of spatial distribution of the source and reservoir, it belongs to the bottom-generation and up-accumulation type of source and reservoir configuration. Hydrocarbons are generated from the Taiyuan-Shanxi Formation and accumulate in the Shanxi-Shihezi Formation.

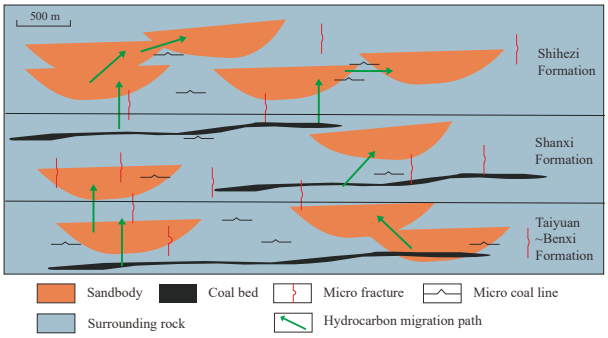

Fig. 2. Accumulation pattern of Sulige Gas Field in the Ordos Basin. Hydrocarbons are generated from the Taiyuan-Shanxi Formation and accumulate in the Shanxi-Shihezi Formation (Liu et al., 2008).

3. Methods

3.1 Accumulation mode

The Taiyuan Formation and Shan-2 Member reservoir are vertically close to the underlying source rock. Meanwhile, the Shan-1 Member and He-8 Member are vertically far from the source rock, and the transport system composed of pores and microfractures plays a highly important role in fluid transport. Driven by the overpressure of hydrocarbon generation in the bottom source rock, hydrocarbons migrated to the Shan-1 Member and He-8 Member along the network transport path and accumulated in relatively high-quality reservoirs. With the replenishment of the lower gas source, hydrocarbons gradually migrated to and accumulated in the upper He-8 Member reservoir (Fig. 2).

Driven by hydrocarbon-generated expansive forces, natural gas charges and migrates to reservoirs along the transport system, then accumulates. Before hydrocarbons enter the transport system from the source rock, they must overcome the capillary pressure in the transport system because the rock is hydrophilic.

Unlike in conventional resources, the dynamic force (buoyancy) in conventional reservoirs is directional; buoyancy gives hydrocarbons a vertical upward force to migrate. However, in

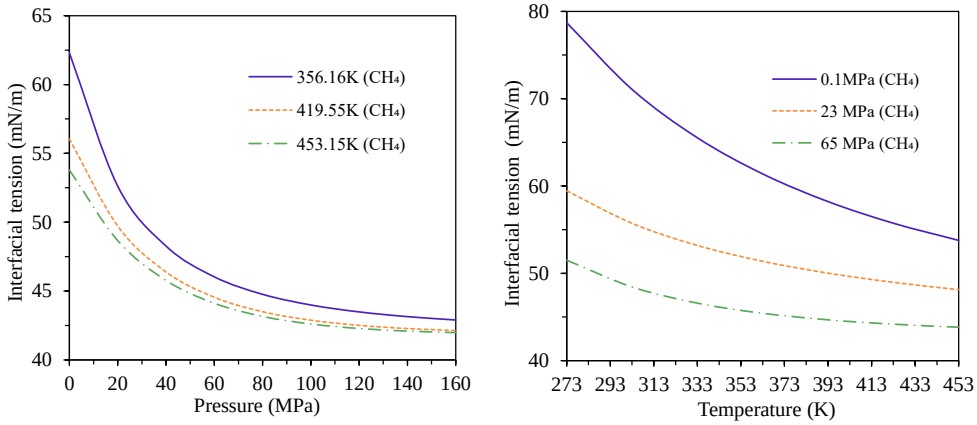

Fig. 3. IFT of the CH_4 and water system under different (a) pressures and (b) temperatures.

tight reservoirs, the hydrocarbon-generated expansive force is not directional, which makes the process and mechanism of natural gas migration in tight reservoirs differ greatly from those in conventional reservoirs.

The dynamic force (hydrocarbon generation expansive force) and the resistance (capillary force) that occur during tight gas accumulation are directionless forces. Therefore, the migration path of tight sandstone gas shows strong heterogeneity during the charging and migration process. Under the control of micro-heterogeneous capillary forces in pores, natural gas tends to migrate along paths with relatively small capillary forces in macro-homogeneous formations.

3.2 Dynamic mechanism of accumulation

A critical requirement for gas charging is high enough gas phase pressure to displace water from the formation. The threshold capillary pressure (P_g) for the gas phase is given as:

$$P_{ca} = P_g - P_w = \frac{2\sigma\cos\theta}{r} \tag{1}$$

where P_{ca} denotes the capillary force, P_w denotes the water pressure, P_g denotes the gas pressure, r denotes the radius of the pore throats, σ denotes the water/methane interfacial tension and θ denotes the contact angle of the methane/water/rock system. In Eq. (1), the interfacial tension (IFT) σ and contact angle θ are two key parameters used to determine the threshold capillary force.

The pressure- and temperature-dependent water/methane interfacial tension σ_{gw} has been proposed in previous work (Jiang et al., 2021):

$$\sigma_{gw} = A(\rho_w - \rho_g)^B T_r^C + D \tag{2}$$

In this semi-empirical model, A, B, C, and D are four constants that depend on the gas properties. Their values are $A = 82.61$, $B = 6.64$, $C = -2.25$, $D = 41.85$ in Eq. (2), and natural gas density ρ_g and water density ρ_w are also pressure- and temperature-dependent properties.

Natural gas density. The natural gas density under different pressures and temperatures is calculated by the equation of state (Wu et al., 2016):

$$\rho_g(P,T) = \frac{PM}{ZRT} \tag{3}$$

where M represents the gas molar mass, and its value for methane is 16×10^{-3} kg/mol; R denotes the gas constant, which equals 8.314 J/(Kmol); Z is the gas deviation factor.

The gas deviation factor in Eq. (3) can be estimated by (Wu et al., 2016):

$$Z = 1 + \frac{P_r}{10.24T_r}\left[2.16\left(\frac{1}{T_r^2} + \frac{1}{T_r}\right) - 1\right] \tag{4}$$

$$P_r = \frac{p}{P_c}, \quad T_r = \frac{T}{T_c} \tag{5}$$

where P_c and T_c represent the critical pressure and temperature, and P_r and T_r represent the reduced pressure and temperature, respectively.

Water density. The density of water is expressed as a function of pressure and temperature (Zhou et al., 2017):

$$\rho_w = \frac{\rho_{w,0}}{1 + \beta\,(T_1 - T_0)} \frac{E}{E - (P - P_0)} \tag{6}$$

Fig. 3(a) illustrates the variation in CH_4/water interfacial tension under different pressures. Under identical temperature conditions, with increasing pressure, the interfacial tension decreases. At $T = 419.55$ K (the average temperature during the natural gas charging process), when the pressure increases from 0.1 (the atmospheric pressure) to 23 MPa (the present reservoir pressure), the interfacial tension decreases from 55.99 to 49.08 mN/m, which is a decrease of approximately 12.34%.

Fig. 3(b) shows the variation in CH_4/water interfacial tension at different temperatures under the identical pressure condition of $P = 23$ MPa (the present reservoir condition). With increasing temperature, the interfacial tension tends to decrease. When the temperature increases from 293 (the standard temperature) to 256.15 K (the present reservoir condition), the interface tension decreases from 56.81 to 51.75 mN/m (8.91%). The CH_4/water interfacial tension decreases with increasing temperature and pressure.

Furthermore, a calculation method for the pressure- and

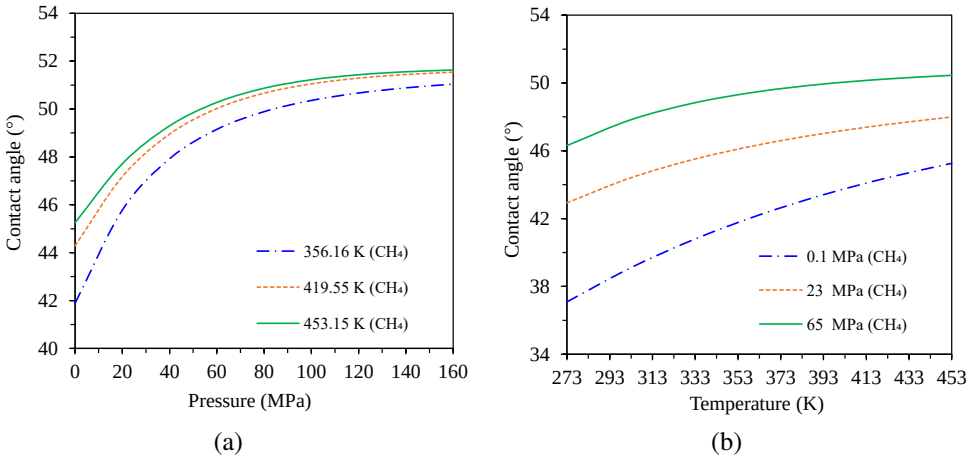

Fig. 4. Contact angle variation under different (a) pressures and (b) temperatures.

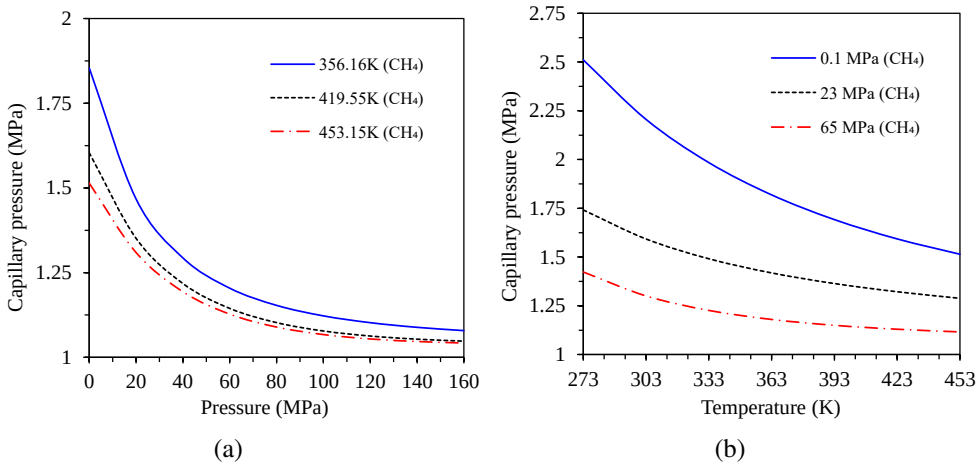

Fig. 5. Capillary pressure under different pressures and temperatures at the pore radius of 50 nm. (a) The relationships between capillary pressure and pressure condition and (b) the relationships between capillary pressure and temperature.

temperature-dependent contact angle (wettability) is proposed based on the DLVO theory (Jiang et al., 2021):

The contact angle can be calculated by:

$$\cos\theta = 1 - \frac{H_{vdW}}{24\pi\sigma f^{*2}} \tag{7}$$

where f^* denotes the film thickness, and H_{vdW} is the Hamaker constant for the interactions between the gas/water system. These constants are calculated based on the refractive index and the dielectric permittivity of the interface (Israelachvili, 2011).

As shown in Fig. 4(a), under the present reservoir pressure ($P = 23$ MPa), when the temperature increases from 356.15 to 419.55 K, the contact angle increases from 45° to 48° by approximately 6.67%. In Fig. 4(b), under the present reservoir temperature ($T = 356.16$ K), when the pressure increases from 23 to 65 MPa, the contact angle increases from 45° to 49° by approximately 8.89%. Notably, the contact angle increases with rising pressure and temperature, which indicates that the formation is less hydrophilic (or more hydrophobic) when gas is charged into the formation.

As shown in Figs. 3 and 4, combined with Eq. (1), the relationships between capillary pressure and the temperature and pressure condition can be revealed (Fig. 5). Under the current condition, the temperature condition is 356.16 K. When the pressure increases from 20 to 60 MPa, the capillary pressure decreases from 1.47 to 1.20 MPa by approximately 20%. Under the environmental pressure of 0.1 MPa, when the temperature increases from 303 to 363 K, the capillary pressure decreases from 2.21 to 1.81 MPa by approximately 18%. The increase in both the environmental pressure and temperature lead to a decline in capillary pressure, which means that natural gas can be charged into the reservoir more easily.

3.3 Numerical simulation methods

In this section, a numerical simulation method is proposed to narrow the gap between theory and field application. The pressure- and temperature-dependent capillary pressure theory will be embedded in the pore network model (PNM) simula-

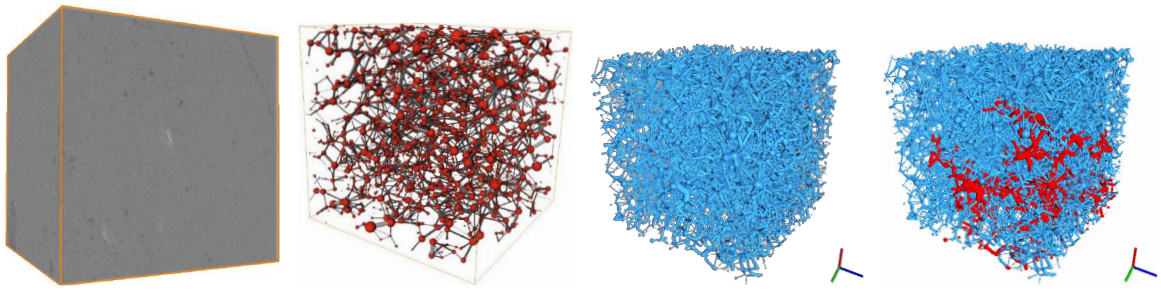

(a) (b) (c) (d)

Fig. 6. A typical PNM model, in which (a) indicates the CT data body; (b) indicates the generated pore network model; (c) represents the condition under which all pores are saturated by water and (d) represents the condition under which natural gas is charged from the bottom. Blue indicates water and red indicates natural gas.

tion, the effect of the microscopic mechanism will be revealed by PNM simulation, and the reservoir scale will be investigated by geological simulation.

3.3.1 Pore network model for core scale

Pore network models are mainly divided into two types: Quasi-steady state and dynamic state models. The former ignores viscous forces during the flow process, and the displacement process and fluid distribution in each pore are controlled by capillary forces. The saturation in each pore does not change as long as the magnitude of capillary force remains constant. The dynamic model is suitable for the study of two-phase fluid systems in which both capillary and viscous forces are important factors. It can simulate the fluid injection process at a constant pressure or constant flow rate. The dynamic model is realized by solving the pressure field of the entire pore network, and then gradually updating the fluid parameters and phase states in the model. The dynamic state model is adopted in this work. Fig. 6 illustrates a typical PNM model, where blue indicates water and red indicates natural gas; Fig. 6(a) shows the computed tomography (CT) data body, where the matrix and pore are distinguished by density differences; Fig. 6(b) presents the generated pore network model, where the sphere represents the pore, and its diameter represents the size of the pore. The cylinder represents the throat, and its length and diameter represent the length and size of the throat, respectively; Fig. 6(c) represents the condition under which all pores are saturated by water and Fig. 6(d) represents the condition under which natural gas is charged from the bottom, and some pores are saturated with natural gas. The pressure- and temperature-dependent capillary pressure theory is embedded in the PNM.

3.3.2 Method of upscaling from core scale to reservoir scale

In Section 3.2, the pressure- and temperature-dependent capillary force calculation method has been embedded in the pore network model. Thus, the microscopic mechanism can be expressed by core scale numerical simulation. The accumulation of hydrocarbons in tight formations is a typical self-sealing phenomenon (Jia et al., 2023). Hydrocarbon migration is a multiphase flow process that can be described by the relative permeability curve (Zhao et al., 2020). A typical gas/water relative permeability curve in tight formation is shown in Fig. 7(a). The Y-axis represents dimensionless permeability, which is normalized by the single phase (gas) permeability, and the X-axis corresponds to the water saturation in tight formations. The red line represents the gas curve; with increasing water saturation, the gas percolation capacity in the formation decreases. The blue line represents the water curve; with increasing water saturation, the water percolation capacity in the formation increases. The hydrocarbon accumulation process is mainly controlled by capillary forces, which can be described by the capillary force curve in tight formations (Zhao et al., 2021). A typical gas/water capillary force curve in tight formations is shown in Fig. 7(b). The Y-axis corresponds to the capillary pressure that the gas has to overcome to enter a pore, and the X-axis represents water saturation. During the charging process, natural gas first tends to enter large pores characterized by low capillary force, and with increasing gas saturation (decreasing water saturation), natural gas has to overcome the higher capillary force of small pores.

Both the relative permeability curve and capillary force curve can be obtained by the PNM method based on a digitized core. In this work, these two curves are proposed to achieve upscaling from the core scale to the reservoir scale.

3.3.3 Geological simulation and reserve evaluation at the reservoir scale

The reservoir of Sulige gas field has the obvious characteristics of "dual structure" (He et al., 2022). According to its heterogeneous characteristics, this reservoir can be divided into two parts: "gas-bearing sand body" and "tight matrix". The "dual structure" reservoir characteristics in the Sulige area are presented in Fig. 8, where yellow represents the gas-bearing sand bodies and grey represents the tight matrix. Table 1 shows the physical characteristics of the dual-structure reservoir. Although the individual size of the main gas-bearing sand body is generally small (with a thickness of 2-5 m and transverse distribution of several hundred meters), a well can be drilled into 2-3 main gas-bearing sand bodies, and the drilling rate and drilling thickness are generally about $1/3^{rd}$ of the total sand body. Although the main gas-bearing sand bodies show dispersed multi-layer dispersed distributions, the

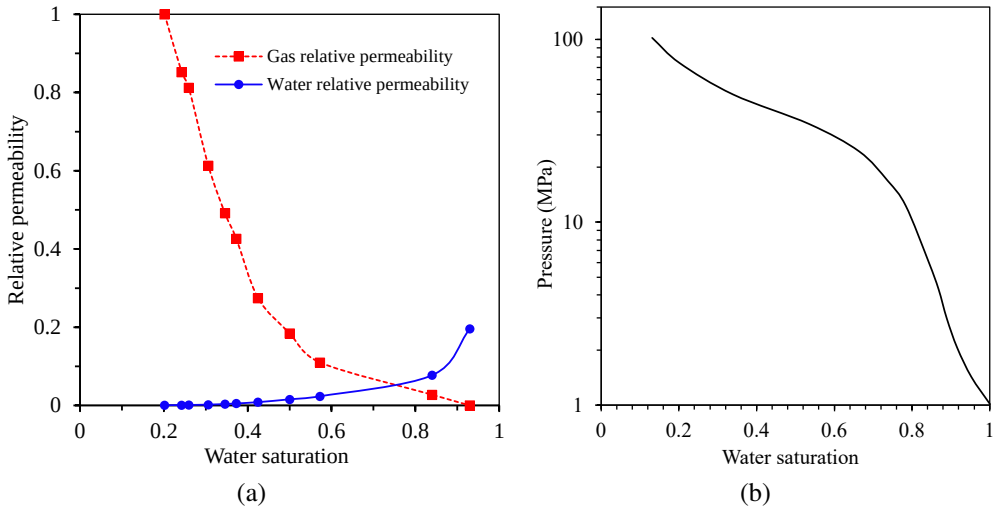

Fig. 7. Typical relative permeability and capillary curves in a tight formation: (a) a gas/water relative permeability curve and (b) a gas/water capillary pressure curve.

Table 1. Physical characteristics of dual-structure reservoirs.

Dual structure	Porosity (%)	Permeability (mD)	Gas saturation (%)	Lithofacies
Gas-bearing sand	5-12	0.1-1.0	55-65	Coarse sandstone
Tight matrix	3-5	< 0.1	30-40	Medium-fine sandstone

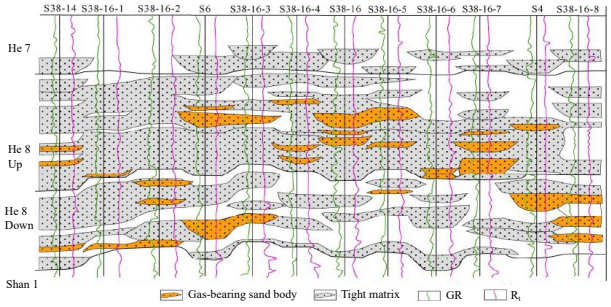

Fig. 8. Characteristic section of reservoir "dual structure" in the Sulige area. Yellow represents the gas-bearing sand bodies and grey represents the tight matrix (Jia et al., 2017).

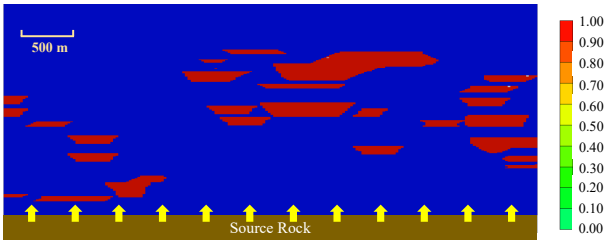

Fig. 9. Geological profile based on the "dual structure" theory. Blue indicates the surrounding tight matrix and red indicates the sand bodies. Natural gas is generated from the source rock, it migrates into the formation and accumulates in the sand bodies.

main gas-bearing sand bodies basically cover all areas of the gas field based on the superposition principle. This is also the reason why the Sulige gas field exhibits overall gas bearing characteristics.

Based on the hydrocarbon accumulation mode discussed in Section 2 and the "dual structure" characteristic of the Sulige tight gas field, the main reservoir geological model can be established, as seen in Fig. 9, where blue indicates the surrounding tight matrix, and red indicates the sand bodies. Natural gas is generated from the source rock, it migrates into the formation and accumulates in sand bodies. A digitized 3D geological digital geological model can also be built (Fig. 10). To make the model more conspicuous, in the image, the surrounding matrix is transparent, and red color is used to represent the sand bodies. The yellow arrows indicate that natural gas will be charged from the bottom. The bottom layer of the grid represents the source rock with an initial pressure of 75 MPa, and gas is charged up from these cells. Reservoir initial conditions are shown in Table 2.

The pressure of source rock is calculated by fluid inclusion analysis (Liu, 2008). Since all properties in the 3D geological model are digitized, it is easy to obtain parameters such as gas saturation, water saturation, gas migration streamlines, pressure distribution during natural gas charging processes and reserve.

4. Results and discussion

4.1 Natural gas charging process

In the simulation process of natural gas charging in a tight sandstone pore network, the main driving force is the source-reservoir pressure difference, and the main resistance is the

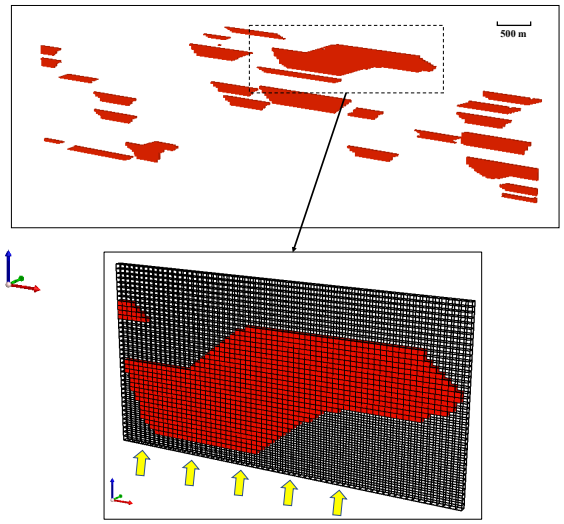

Fig. 10. Digitized 3D geological model. The surrounding tight matrix is transparent, while red represents sand bodies. The yellow arrows indicate that the natural gas will be charged from the bottom.

capillary force of the reservoir. Driven by this pressure difference, natural gas can overcome capillary pressure and is charged into the pores of the reservoir (Zhao et al., 2022).

Under the initial conditions, the pore network model is first saturated with water. Subsequently, natural gas is charged into the pore network model from the bottom. The simulation in this paper realizes the visual representation of the results, as shown in Fig. 11(a). To observe the gas charging process and distribution characteristics more clearly, the pores that were not filled with natural gas (those still full of water) are not shown in Fig. 11, and the pores and throats that were filled with gas are shown in red. The geometric structural features of the pore network are retained (a sphere represents a pore and its diameter represents pore size; a cylinder represents a throat, and its length and diameter represent the length and width of the throat).

At the initial stage of gas charging, when the gas saturation is 10% (Fig. 11(a)), gas first enters the pore network through the larger, connected pores and generates the charging front (region A in Fig. 11(a)). Although some pores at the bottom are also filled with gas, they cannot be pushed forward immediately after gas filling because of the small size of the throat connected to them and the high capillary resistance (region B in Fig. 11(a)).

As the charging progresses, more gas enters the pore network and the gas saturation increases. At this time, the gas in region B in Fig. 11(a) continues to advance (blue arrow in region B in Fig. 11(b)) and connects with part of the gas in region C in Fig. 11(b). At this time, the gas advances through the hyperpermeability channel composed of larger pores and throats. A new charging front (area D in Fig. 11(b)) is formed, and the natural gas flow pattern in the charging process presents "fingering" features.

The gas saturation further increases, and when it reaches 50%, the larger pores are essentially completely charged (Fig. 11(c)). It is worth noting that because of the heterogeneity of the pore network, not all macropores will be charged first. For macropores connected with small pores or narrow throats, gas can be charged only after the connected small pores or narrow throats have been charged in the late charging period (Fig. 11(d)), or they will not be charged at all.

Table 2. Physical characteristics of dual-structure reservoirs.

Reservoir condition	Value
Reservoir depth (m)	2000
Initial reservoir temperature (°C)	40
Initial reservoir pressure (MPa)	20
Source rock pressure (MPa)	65

4.2 Natural gas migration process

In tight formations, natural gas is generated from the source rock. Driven by the expansion force of hydrocarbon generation, gas is charged and migrates in the reservoir. Fig. 12 shows the natural gas migration streamline, where the red lines represent sand bodies, and the blue lines represent the flow path. Dense spacing means greater flow velocity, and the streamline direction indicates the direction of gas flow. At the edge of sand bodies, the streamlines tend to be bent. At the lower edge, at the macroscopic level, gas migrates from the surrounding rock to the sweet spot; at the microscopic level, gas bubbles migrate from small pores to large pores. Meanwhile, at the upper edge, at the macroscopic level, gas migrates from the sweet spot to the surrounding rock; at the microscopic level, gas bubbles migrate from large pores to small pores.

The difference in streamlines indicates the variation in migration dynamics, which lead to differences in gas saturation. Fig. 13 shows the gas saturation distribution during the gas migration processes, where black lines indicate sand bodies, red indicates high gas saturation, and green indicates low gas saturation. The natural gas migrates faster in the sand bodies that have larger porosity and permeability.

Similar to the distribution of gas saturation, Fig. 14 depicts the pressure distribution during the natural gas charging process, where black lines indicate sand bodies, red indicates high pressure, and blue indicates low pressure. The pressure of gas is the highest as it leaves the source rock, and decreases as it is charged upward. The pressure reduction occurs faster as the gas passes through the surrounding tight matrix and it occurs slower as it passes through sand bodies.

4.3 Natural gas accumulation and reserve evaluation

Fig. 15 presents the natural gas accumulation stage of Shihezi Formation and Shanxi Formation in the Sulige gas field. Shihezi Formation and Shanxi Formation formed hydrocarbon reservoirs, which lasted from the end of the Middle Triassic (approximately 220 Ma) to the end of the Early Cretaceous (approximately 100 Ma), spanning 120 Ma. During this time, hydrocarbon charging occurred continuously, but the intensity of charging was different. The accumulation period can be

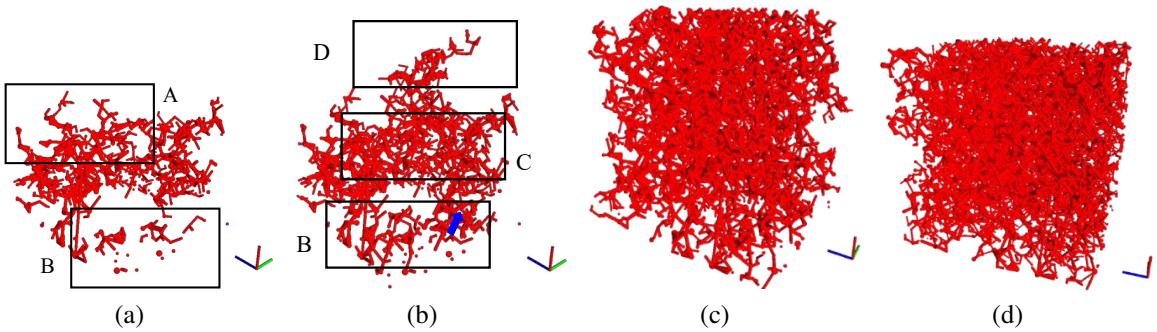

Fig. 11. Natural gas distribution during the charging processes with gas saturations of (a) 10%, (b) 20%, (c) 50% and (d) 70%.

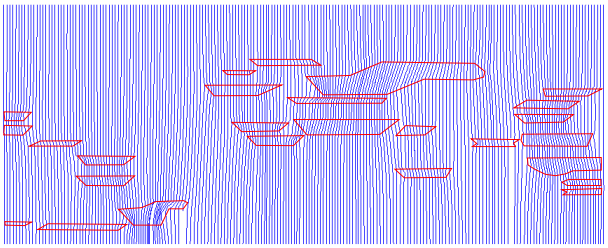

Fig. 12. Natural gas migration streamlines. Red lines indicate sand bodies, while blue lines represent the flow path. Dense spacing means greater flow velocity.

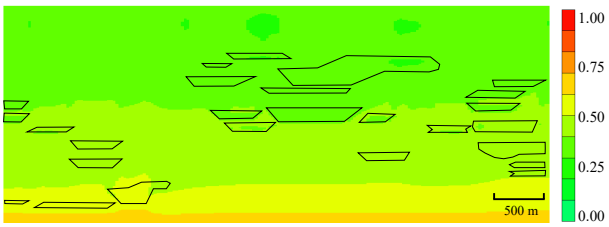

Fig. 13. Snapshot of gas saturation distribution. Black lines indicate sand bodies, red indicates high gas saturation, and green indicates low gas saturation. Natural gas migrates faster in sand bodies that have greater porosity and permeability.

divided into two stages: initial charging period and main charging period. By combining Fig. 15 and the temperature-pressure capillary calculation method, the obtained formation temperature is 443.15 K, and the pressure is 60 MPa in the maximum burial environment; the obtained formation temperature is 358.15 K, and the pressure is 40 MPa in the initial charging environment; the obtained formation temperature is 333.15 K, and the pressure is 23 MPa at the present burial depth (As shown in Table 3). Under different temperature and pressure conditions, the capillary curve is also different. Compared to the present burial depth environment, the capillary force under the initial charging environment is 13% lower, and the capillary force under the maximum burial environment is 25% lower. In high-pressure and high-temperature environments, the capillary force markedly decreases, which means that natural gas can be charged into pores more easily; gas saturation increases under high-pressure and high-temperature conditions.

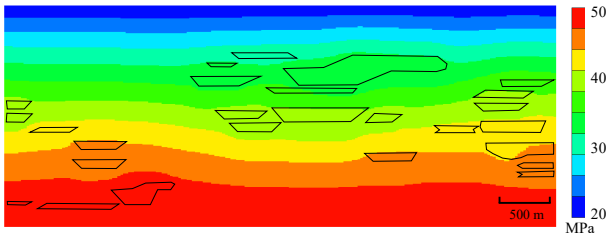

Fig. 14. Pressure distribution during natural gas charging processes. Black lines indicate sand bodies, red indicates high pressure, and blue indicates lower pressure. The pressure of gas is the highest as it leaves the source rock, and it decreases as it is charged upward. The pressure reduction is faster when the gas passes through the surrounding tight matrix and it is slower when it passes through sand bodies.

For instance, the capillary force that natural gas needs to overcome during the charging process in 50 nm pores varies under different environments (Fig. 16). In the present burial depth environment, the capillary pressure in a 50 nm pore that natural gas must overcome during the charging process is 1.49 MPa; under the initial charging environment, this capillary pressure is 1.28 MPa, (decrease of 14.1%); under the maximum burial environment, this capillary pressure is 1.11 MPa, which is an approximately 25.5% decrease compared to the present burial depth environment. Fig. 17 illustrates the relationship between the pore size distribution and charged pores under different environmental conditions. The Y-axis corresponds to the pore size distribution frequency, and the X-axis indicates pore size, with smaller pores on the left, and larger pores on the right. Different colors indicate the different ranges of pore-throats that can be filled in the maximum burial environment, initial charging environment, and present burial depth. It is found that, at the same charging pressure, under the present burial depth, only the blue area could be charged; under initial charging, both the green and the blue area could be charged, and under the maximum burial environment, all of the red, green and blue areas could be charged. The sand body in the lower part of Fig. 10 is taken as an example for analysis, and Table 4 shows the reserve of this sand body under different accumulation environments. Under higher pressure and temperature conditions, at the same charging pressure, natural gas can be charged into smaller pores, and the sand body has higher gas saturation and reserves.

Table 3. Formation temperature and pressure in the numerical simulation.

Environment	Pressure (MPa)	Temperature (K)	IFT (mN/m)	Contact angle (°)	Capillary pressure* (MPa)
Maximum burial depth	65	443.15	43.94	50.39	1.11
Initial charging period	40	358.15	48.00	48.07	1.28
Present burial depth	23	333.15	53.20	45.52	1.49

* in 50 nm pore.

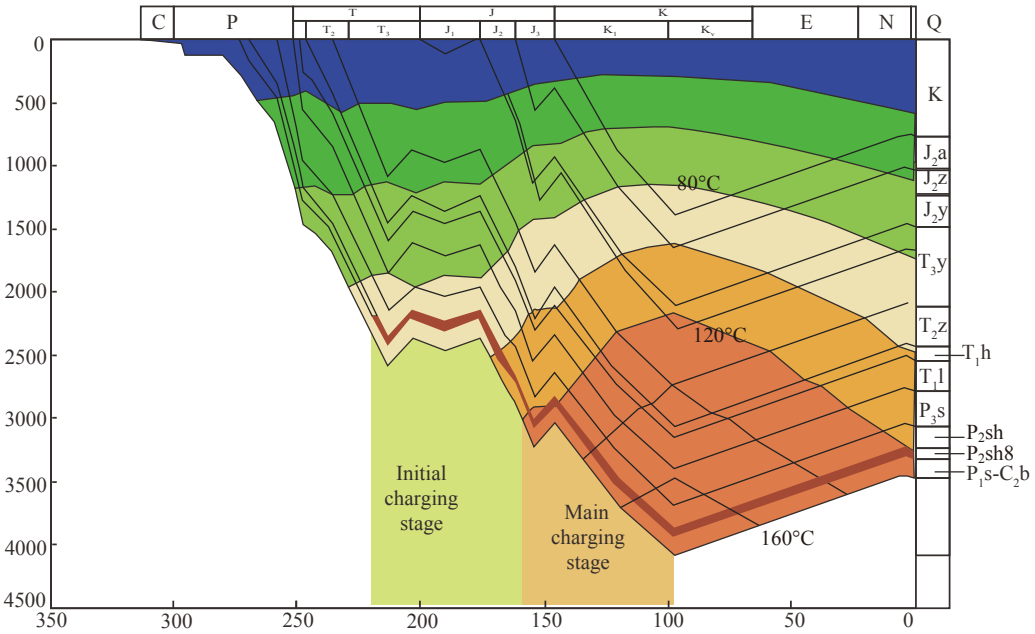

Fig. 15. Natural gas accumulation stage of Shihezi Formation and Shanxi Formation in the Sulige gas field. In one stage, the Shihezi Formation and Shanxi Formation formed hydrocarbon reservoirs, which lasted from the end of the Middle Triassic (approximately 220 Ma) to the end of the Early Cretaceous (approximately 100 Ma), spanning 120 Ma, during which hydrocarbon charging occurred continuously, but the intensity of charging was different (Han et al., 2020).

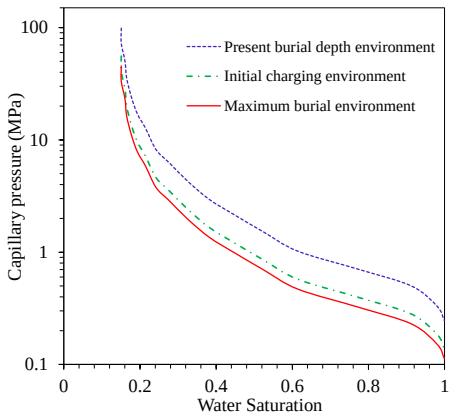

Fig. 16. Capillary pressure curves under different environmental conditions.

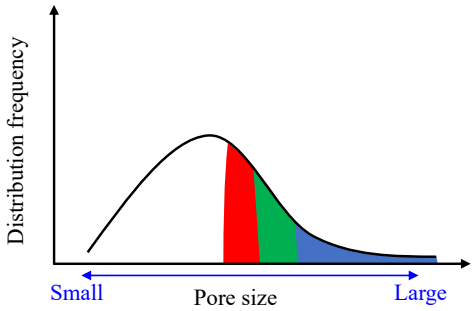

Fig. 17. Relationship between pore size distribution and charged pores under different environmental conditions.

5. Conclusions

This work reveals the tight gas migration and accumulation mechanisms and proposes numerical simulation methods for tight formations. Based on the micro-scale dynamic mechanisms, the gap between theory and field applications is narrowed. The main conclusions are summarized as follows:

1) The self-sealing effect of capillary pressure in micro/nanopore throat systems is at the core of tight sandstone gas accumulation theory. The driving force is the hydrocarbon-generated expansion force, and the resistance is the capillary force.
2) Microscopic capillary force studies can be embedded into

Table 4. Reserve of typical sand body.

Accumulation environment	Porosity (%)	Permeability (mD)	Pore volume (m^3)	Gas saturation	Reserve ($\times 10^4\ m^3$)
Present burial depth	5.33	0.13	4436	0.57	77
Initial charging period	5.33	0.13	4436	0.65	87
Maximum burial depth	5.33	0.13	4436	0.76	102

pore network model and scaled up by combining the relative permeability curve and capillary force curve in the geological model. Meanwhile, field applications can be achieved by geological numerical simulations at the reservoir scale.

3) High temperatures and pressures can reduce capillary pressure, increasing gas saturation and reserves, which should be taken into account in resource assessment and sweet spot prediction.

Acknowledgements

This work was supported by CNPC Scientific Research and Technology Development Project "Whole petroleum system theory and unconventional hydrocarbon accumulation mechanism" (No. 2021DJ0101).

Conflict of interest

The authors declare no competing interest.

References

Abukova, L. A., Volozh, Y. A., Dmitrievsky, A. N., et al. Geofluid dynamic concept of prospecting for hydrocarbon accumulations in the Earth crust. Geotectonics, 2019, 53: 372-382.

Algarhy, A., Ibrahim, A. F. Application of machine learning to predict the organic shale sweet-spot quality index. Paper SPE 211889 Presented at SPE Eastern Regional Meeting, Wheeling, West Virginia, USA, 18-20 October, 2022.

Berry, F. A. Theory of osmosis and ion-exclusion by semipermeable membranes, in Hydrodynamics and Geochemistry of the Jurassic and Cretaceous Systems in the San-Juan Basin, Northwestern New Mexico and Southwestern Colorado, edited by F. A. Berry, Stanford University ProQuest Dissertations Publishing, San Francisco, pp. 165-168, 1959.

Blanchard, K. S., Denman, O., Knight, A. S. Natural gas in Atokan (Bend) section of northern Fort Worth basin. AAPG Bulletin, 1968, 30(2): 1379-1388.

Blunt, M. J. Introduction to reservoir engineering, in Imperial College Lectures in Petroleum Engineering, The-Volume 2: Reservoir Engineering, edited by M. J. Blunt, World Scientific Publishing Company, London, pp. 22-23, 2017.

Budd, H. Developments in Arizona and Western New Mexico in 1958. AAPG Bulletin, 1959, 43(6): 1379-1388.

Burrows, L. C., Haeri, F., Cvetic, P., et al. A literature review of CO_2, natural gas, and water-based fluids for enhanced oil recovery in unconventional reservoirs. Energy & Fuels, 2020, 34(5): 5331-5380.

Cluff, R. M., Byrnes, A. P. Relative permeability in tight gas sandstone reservoirs-the permeability jail model. Paper SPWLA 2010 58470 Presented at SPWLA 51st Annual Logging Symposium, Perth, Australia, 19-23 June, 2010.

Davis, T. B. Subsurface pressure profiles in gas-saturated basins. AAPG Special Volume, 1984, 9(38): 189-203.

Emmons, W. H. Experiments on accumulation of oil in sands. AAPG Bulletin, 1921a, 5(1): 103-104.

Emmons, W. H. Subsurface geology, in Geology of Petroleum, edited by A. I. Levorsen, McGraw-Hill Book Company, New York, USA, pp. 610-615, 1921b.

Fassett, J. E. Oil and gas resources of the San Juan basin, New Mexico and Colorado, in Economic Geology, US, edited by H. J. Gluskoter, D. D. Rice and R. B. Taylor, Geological Society of America, Boulder, pp. 357-372, 1991.

Fassett, J. E., Hinds J. S. Geology and Fuel Resources of the Fruitland Formation and Kirtland Shale of the San Juan basin, New Mexico and Colorado. Washington, USA, US Government Printing Office, 1971.

Gholami, A., Amirpour, M., Ansari, H. R., et al. Porosity prediction from pre-stack seismic data via committee machine with optimized parameters. Journal of Petroleum Science and Engineering, 2022, 210: 110067.

Han, Z., Zhao, J., Chen, M., et al. Fluid inclusion characteristics and hydrocarbon accumulation period of He 8 member reservoir in the western area of Sulige Gasfield. Journal of Xi'an Shiyou University (Natural Science Edition), 2020, 35(1): 18-27. (in Chinese)

He, J., Yu, H., He, G., et al. Natural gas development prospect in Changqing gas province of the Ordos Basin. Natural Gas Industry B, 2022, 9(2), 197-208.

Hentz, T. F. Sequence stratigraphy of the upper Pennsylvanian Cleveland Formation: A major tight-gas sandstone, western Anadarko basin, Texas Panhandle. AAPG Bulletin, 1994, 78(4): 569-595.

Hills, J. M. Gas in Delaware and Val Verde basins, west Texas and southeastern New Mexico, in Natural Gases of North America, Volume Two, edited by B. W. Beebe, American Association of Petroleum Geologists, Tulsa, pp. 1394-1432, 1968.

Hu, T., Pang, X., Jiang, F., et al. Dynamic continuous hydrocarbon accumulation (DCHA): Existing theories and a new unified accumulation model. Earth-Science Reviews, 2022a, 232: 104109.

Hu, T., Wu, G., Xu, Z., et al. Potential resources of conventional, tight, and shale oil and gas from Paleogene Wenchang Formation source rocks in the Huizhou Depression. Advances in Geo-Energy Research, 2022b, 6(5): 402-414.

Israelachvili, J. N. Contrasts between Intermolecular, Interparticle, and Intersurface Forces, in Intermolecular and Surface Forces (Third Edition), edited by J. N. Israelachvili, Academic Press, California, pp. 205-222, 2011.

Jackson, P. C. Paleogeography of the Lower Cretaceous Mannville group of western Canada, in Elmworth: Case Study of a Deep Basin Gas Field, edited by J. A. Masters, Amer Assn of Petroleum Geologists, Tulsa, pp. 49-77, 1984.

Jia, A., He, D., Wei, Y., et al. Predictions on natural gas development trend in China for the next fifteen years. Journal of Natural Gas Geoscience, 2021, 6(2): 67-78. (in Chinese)

Jia, C., Pang, X., Song, Y. Whole petroleum system and ordered distribution pattern of conventional and unconventional oil and gas reservoirs. Petroleum Science, 2023, 20(1): 1-19.

Jia, A., Wang, G., Meng D., et al. Well pattern infilling strategy to enhance oil recovery of giant low-permeability tight gas field: A case study of Sulige gas field, Ordos Basin. Acta Petrolei Sinica, 2017, 39(7): 802-813. (in Chinese)

Jiang, L., Zhao, W., Huang, J., et al. Effects of interactions in natural gas/water/rock system on hydrocarbon migration and accumulation. Scientific Reports, 2021, 11(1): 22070.

Khalifah, H. A., Glover, P. W. J., Lorinczi, P. Permeability prediction and diagenesis in tight carbonates using machine learning techniques. Marine and Petroleum Geology, 2020, 112: 104096.

Khatibi, S., Ostadhassan, M., Xie, Z. H., et al. NMR relaxometry a new approach to detect geochemical properties of organic matter in tight shales. Fuel, 2019, 235: 167-177.

Law, B. E. Basin-centered gas systems. AAPG Bulletin, 2002, 86(11): 1891-1919.

Li, J., Yang, Z., Wu, S., et al. Key issues and development direction of petroleum geology research on source rock strata in China. Advances in Geo-Energy Research, 2021, 5(2): 121-126.

Lin, D., Wang, J., Yuan, B., et al. Review on gas flow and recovery in unconventional porous rocks. Advances in Geo-Energy Research, 2017, 1(1): 39-53.

Liu, X. The accumulation mechanism of lithologic gas reservoir of the upper Paleozoic in Eastern Ordos Basin. Xi'an, Northwestern University, 2008.

Masters, J. A. Deep basin gas trap, western Canada. AAPG Bulletin, 1979, 63(2): 152-181.

Myers, D. L. Drilling in the deep basin, in Elmworth: Case Study of a Deep Basin Gas Field, edited by J. A. Masters, Amer Assn of Petroleum Geologists, Tulsa, pp. 283-290, 1984.

Pang, X., Jia, C., Wang, W., et al. Buoyance-driven hydrocarbon accumulation depth and its implication for unconventional resource prediction. Geoscience Frontiers, 2021, 12(4): 101133.

Rahmani, R. A. Facies control of gas trapping, Lower Cretaceous Falher A cycle, Elmworth area, northwestern Alberta, in Elmworth: Case Study of a Deep Basin Gas Field, edited by J. A. Masters, Amer Assn of Petroleum Geologists, Tulsa, pp. 141-152, 1984.

Rutter, E., Mecklenburgh, J., Bashir, Y. Matrix gas flow through "impermeable" rocks-shales and tight sandstone. Solid Earth, 2022, 13(3): 725-743.

Sell, B., Murphy, D., Hall, C. A. S. Energy return on energy invested for tight gas wells in the Appalachian Basin, United States of America. Sustainability, 2011, 3(10): 1986-2008.

Shanley, K. W., Cluff, R. M., Robinson, J. W. Factors controlling prolific gas production from low-permeability sandstone reservoirs: Implications for resource assessment, prospect development, and risk analysis. AAPG Bulletin, 2004, 88(8): 1083-1121.

Smith, R. D. Gas reserves and production performance of the Elmworth/Wapiti area of the deep basin, in Elmworth: Case Study of a Deep Basin Gas Field, edited by J. A. Masters, Amer Assn of Petroleum Geologists, Tulsa, pp. 153-172, 1984.

Sneider, R. M., Tinker, C. N., Meckel, L. D. Deltaic environment reservoir types and their characteristics. Journal of Petroleum Technology, 1978, 30(11): 1538-1546.

Soleymanzadeh, A., Kord, S., Monjezi, M. A new technique for determining water saturation based on conventional logs using dynamic electrical rock typing. Journal of Petroleum Science and Engineering, 2021, 196: 107803.

Stayura, J. A. Completion practices in the Alberta deep basin, in Elmworth: Case Study of a Deep Basin Gas Field, edited by J. A. Masters, Amer Assn of Petroleum Geologists, Tulsa, pp. 291-296, 1984.

Thomas, J. D., Texas, W. Integrating synsedimentary tectonics with sequence stratigraphy to understand the development of the Fort Worth basin. Paper SWS AAPG 90023 Presented at AAPG Southwest Section Meeting, Ruidoso, New Mexico, 6-8 June, 2002.

Tissot, B. P., Welte, D. H. Petroleum Formation and Occurrence. Berlin, Germany, Springer-Verlag, 1984.

Wang, R., Liu, K., Shi, W., et al. Reservoir densification, pressure evolution, and natural gas accumulation in the Upper Paleozoic tight sandstones in the North Ordos Basin, China. Energies, 2022, 15(6): 1990.

Wang, R., Shi, W., Xie, X., et al. Clay mineral content, type, and their effects on pore throat structure and reservoir properties: Insight from the Permian tight sandstones in the Hangjinqi area, north Ordos Basin, China. Marine and Petroleum Geology, 2020, 115: 104281.

Wu, K., Li, X., Guo, C., et al. A unified model for gas transfer in nanopores of shale-gas reservoirs: Coupling pore diffusion and surface diffusion. SPE Journal, 2016, 21(5): 1583-1611.

Wu, H., Zhao, J., Wu, W., et al. Formation and diagenetic characteristics of tight sandstones in closed to semi-closed systems: Typical example from the Permian Sulige gas field. Journal of Petroleum Science and Engineering, 2021, 199: 108248.

Zhang, L., Pang, X., Pang, H., et al. Hydrocarbon accumulation model based on threshold combination control and favorable zone prediction for the lower Enping Formation, Southern Lufeng sag. Advances in Geo-Energy Research, 2022, 6(5): 438-450.

Zhao, W., Jia, C., Jiang, L., et al. Fluid charging and hydrocarbon accumulation in the sweet spot, Ordos Basin, China. Journal of Petroleum Science and Engineering, 2021, 200: 108391.

Zhao, W., Wu, K., Jiang, L., et al. Charging and microscopic gas-water occurrence characteristics of tight sandstone gas based on pore network model. Natural Gas Industry, 2022, 42(5): 69-79. (in Chinese)

Zhao, W., Zhang, T., Jia, C., et al. Numerical simulation on natural gas migration and accumulation in sweet spots of tight reservoir. Journal of Natural Gas Science and Engineering, 2020, 81: 103454.

Zhou, Y., Hatzignatiou, D. G., Helland, J. O. On the estimation of CO_2 capillary entry pressure: Implications on geological CO_2 storage. International Journal of Greenhouse Gas Control, 2017, 63: 26-36.